Published in final edited form as:
J Comput Phys. 2013 July 1; 244: 22–40. doi:10.1016/j.jcp.2012.09.016.

Multi-Scale Computational Model of Three-Dimensional Hemodynamics within a Deformable Full-Body Arterial Network

Nan Xiao[a,c], **Jay D. Humphrey**[b], and **C. Alberto Figueroa**[c,*]

[a]Department of Bioengineering, Stanford University, Stanford, CA 94305 USA

[b]Department of Biomedical Engineering, Yale University, New Haven, CT 06520 USA

[c]Department of Biomedical Engineering, King's College London, London SE1 7EH, UK

Abstract

In this article, we present a computational multi-scale model of fully three-dimensional and unsteady hemodynamics within the primary large arteries in the human. Computed tomography image data from two different patients were used to reconstruct a nearly complete network of the major arteries from head to foot. A linearized coupled-momentum method for fluid-structure-interaction was used to describe vessel wall deformability and a multi-domain method for outflow boundary condition specification was used to account for the distal circulation. We demonstrated that physiologically realistic results can be obtained from the model by comparing simulated quantities such as regional blood flow, pressure and flow waveforms, and pulse wave velocities to known values in the literature. We also simulated the impact of age-related arterial stiffening on wave propagation phenomena by progressively increasing the stiffness of the central arteries and found that the predicted effects on pressure amplification and pulse wave velocity are in agreement with findings in the clinical literature. This work demonstrates the feasibility of three-dimensional techniques for simulating hemodynamics in a full-body compliant arterial network.

1. Introduction

Hypertension and aging are primary risk factors for many adverse cardiovascular conditions, including heart attack, stroke, and end-stage renal disease. It is now widely recognized that increased stiffening of the central arteries – that is, the aorta and carotids – is both a cause and a consequence of hypertension [1, 2, 5, 9] and that there is a close association between the increased arterial stiffening of hypertension and that of aging [16, 27, 29, 34]. Because of the strong interactions between the evolving arterial wall properties and associated hemodynamics, there is a pressing need to understand better the roles of biomechanics in the progression of cardiovascular disease as well as to use biomechanics to design better methods of diagnosis, prognosis, and treatment. In particular, hemodynamic metrics such as central artery pulse pressure (cPP), augmentation index (AIx), and carotid-to-femoral pulse wave velocity (CF-PWV) are now thought of as both initiators and indicators of disease and disease susceptibility [25, 29]. It is also becoming increasingly evident, however, that changes in wall mechanics may progress both spatially (e.g., from proximal to distal vessels

*Corresponding author: Address: 3rd Floor Lambeth Wing, St Thomas' Hospital, King's College London, London SE1 7EH, UK, Telephone: +44 771 580 2408, Fax: +44 207 188 5442, alberto.figueroa@kcl.ac.uk.

[31] and temporally (i.e., via biological aging, not just chronological aging [7, 47]). Hence, there is a need to understand how local changes in arterial stiffness can affect local and global hemodynamics. Because of the complex geometry and material properties of the central arteries, and the hemodynamics therein that also depend on effects arising from distal conduit and resistance vessels, large-scale computational models of vascular mechanics are needed to improve our ability to interpret current clinical findings and to advance our fundamental understanding of the mechanisms of disease progression.

There have been several seminal computational studies of hemodynamics within the human arterial network [44, 36, 4, 38, 28, 37, 33, 3]. These studies have described the physics of flow and pressure wave propagation in a one-dimensional (1-D) setting. In this paper, we present the first model of fully unsteady and three-dimensional (3-D) hemodynamics within a deformable network of the primary large arteries, from head to foot, including important effects arising from the distal resistance vessels. This model is built upon previous key advances in multi-scale outflow boundary condition formulations [40, 41], efficient methods for fluid-structure interaction (FSI) [11] and perivascular tissue support [24], and methods for anisotropic field-driven mesh adaptation [35]. Resulting computational findings on local pressure waves promise to allow common clinical measurements such as brachial pressures to be directly related to the more important but less easily measured cPP, which has greater prognostic value [43]. Similarly, computational findings on the effects of changes in wall properties on global metrics such as CF-PWV promise to provide increased insight into relationships between evolving wall properties and the temporal progression of hypertension and aging-related changes in hemodynamics. Finally, detailed information on local pressure and velocity fields promise to enable new mechanobiological hypotheses regarding large artery disease to be formulated and tested. Whereas examination of these and other important areas of vascular therapeutics and biology will be pursued in subsequent works, the primary goal of this work is to set the stage by describing an underlying computational framework and demonstrating the feasibility of building a 3-D full-body model.

The structure of this paper is as follows: After reviewing the medical image data and geometric modeling techniques, we describe the modeling framework, specifically the formulations for outflow boundary conditions, FSI and perivascular tissue support. We then present the methodology adopted for vessel wall material parameter specification and outflow boundary conditions. Then, in the results section, we report detailed hemodynamics in two different arterial models: The first model represents the main arteries in the trunk, including the aorta, subclavians, carotids, mesenterics, celiac circulation, and iliac bifurcation, totaling 36 outflow faces. The second case is a full-body model representing the large arteries of the human body, expanding the trunk model to include the main arteries in the legs, arms, and head, for a total of 82 outflow faces. In the first model we highlight the simulation results such as regional blood flow, pressure and flow waveforms, and pressure wave propagation down the aorta. We also present a study of the impact of age-related arterial stiffening on cPP and PWV. We conclude by discussing on the progress made thus far in the field of multi-scale computational modeling of arterial hemodynamics, on the need for techniques to measure pressure, flow and in vivo tissue mechanical parameters required by the ever more sophisticated computational models, and on the potential of computational modeling to identify improved indicators of early stiffening that may allow earlier therapeutic interventions.

2. Methods

2.1. Image Data and Anatomical Reconstruction

To reconstruct a nearly complete network of the major arteries from the head to the lower legs, we combined Computed Tomographic Angiography (CTA) image data from two

different patients. Two datasets were used to obtain full coverage of the body from head to foot The first image was acquired from a relatively healthy adult subject and encompasses the major arteries of the head and neck. The second image volume is a neck-to-lower leg CTA scan of a subject with peripheral vascular disease and encompasses the major arteries below the neck, including those in the torso, arms, and legs. The head CTA consisted of a 512 × 512 × 709 voxel image with a resolution of 0.35 mm × 0.35 mm × 0.5 mm. The neck-to-lower leg CTA consisted of a 512×512×1479 voxel image with a resolution of 0.89 mm × 0.89 mm × 0.89 mm. We reconstructed separate geometric models from each image volume using a segmentation procedure whereby the arterial lumen boundary is defined using a combination of manual demarcation, image thresholding, and level-set segmentation [48]. A set of vessel centerline paths and 2-D segmentations along each path are produced; from these a 3-D geometric solid model is created. The final 3-D geometry was assembled by scaling (due to a height difference between the patients), translating, and finally combining the two separate 3-D models so that the common carotid and vertebral arteries are connected in a smooth and continuous fashion (see Figure 1).

The neck-to-lower-body image of the subject with peripheral vascular disease revealed areas of significant stenosis in the iliac and femoral arteries. In the interest of reproducing hemodynamic features representative of a healthy individual, the narrowed regions were dilated while keeping the relative calibers of the leg vessels consistent with reported dimensions used in previous 1-D blood flow models [33]. Mesh generation is always an important task when dealing with anatomically complex 3-D domains, and it is critical in this case due to the scale and the large range of vessel diameters within the model (2.92 mm diameter at the level of the aortic root versus 0.2 mm diameter at the tibial artery). We adopted a two-step mesh generation strategy whereby a first stage of arbitrarily-specified local curvature-based refinement is followed by a field-driven mesh refinement stage based on steady-flow computations. In the first stage, the parameters of the local curvature-based refinement (MeshSim, Simmetrix, Inc. Clifton Park, NY USA) were chosen to enhance spatial resolution in the smaller branch vessels. Then, the field-based mesh refinement process [35] adapted the mesh to increase element density in the directions of high velocity gradients (see Figure 2).

2.2. Methods for Blood Flow Simulation

2.2.1. Multi-scale modeling approach—We employed the coupled multi-domain method [40], an approach that is based on the Dirichlet-to-Neumann and variational multi-scale methods. Briefly, the coupled multi-domain method employs a disjoint decomposition of the spatial domain $\tilde{\Omega}^f$ into an upstream "numerical" domain Ω^f and a downstream "analytical" domain Ω'^f such that $\tilde{\Omega}^f = \overline{\Omega^f \cup \Omega'^f}$ and $\Omega^f \cap \Omega'^f = \varnothing$. These two domains are separated by the interfaces Γ_{in} and Γ_{out} [10]. Here, Ω^f corresponds to the 3D geometry reconstructed from medical image data in which the Navier-Stokes equations for an incompressible Newtonian fluid are applied. Ω'^f corresponds to the distal vascular networks and microcirculation not included in the 3D geometric model and whose physics are described using simpler theories such as 1D or lumped-parameter formulations. A similar disjoint decomposition is applied to the solution $\tilde{\boldsymbol{V}} = \{\tilde{\boldsymbol{v}}, \tilde{p}\}$: $\tilde{\boldsymbol{V}} = \boldsymbol{V} + \boldsymbol{V}'$ with $\boldsymbol{V}|_{\Omega'^f} = 0$ and $\boldsymbol{V}'|_{\Omega^f} = 0$ and $\boldsymbol{V} = \boldsymbol{V}'$ at the interface Γ_{out}. The unit normals at the interface Γ_{out} are such that $\boldsymbol{n}^f = -\boldsymbol{n}'$. Here, $\tilde{\boldsymbol{v}}$ is the velocity and $\tilde{p}$ the pressure in the spatial domain. In the context of a stabilized finite element formulation with equal-order interpolation functional spaces for velocity and pressure, the variational equation for the blood flow problem is[45]:

$$\begin{aligned}&\int_{\Omega^f}\{\boldsymbol{w}\cdot(\rho^f\,\dot{\boldsymbol{v}}+\rho^f\boldsymbol{v}\nabla\boldsymbol{v}-\boldsymbol{b})+\nabla\boldsymbol{w}:(-p\boldsymbol{I}+\boldsymbol{\tau})-\nabla q\cdot\boldsymbol{v}\}d\boldsymbol{v}\\&+\int_{\Gamma_{\text{in}}}q\boldsymbol{v}\cdot\boldsymbol{n}^f da+\int_{\Gamma_{\text{out}}}\{\boldsymbol{w}'\cdot(-p'\boldsymbol{I}+\boldsymbol{\tau}')-q'\boldsymbol{v}'\}\cdot\boldsymbol{n}'da\\&+\int_{\Gamma_t}\{-\boldsymbol{w}\cdot\boldsymbol{t}^f+q\boldsymbol{v}\cdot\boldsymbol{n}^f\}da+\text{stabilization terms}=0\\&\forall\boldsymbol{x}(t)\in\overline{\Omega^f},\forall t\in[0,T].\end{aligned}\tag{1}$$

Here, q and q' and $\boldsymbol{w}$ and $\boldsymbol{w}'$ are the test functions for mass and momentum balance in Ω^f and Ω'^f, respectively, and ρ^f is the blood density. Γ_{in} is a Dirichlet boundary where the test functions $\boldsymbol{w}$ vanish. Γ_t is the boundary of Ω^f representing the interface with the arterial wall where a traction $\boldsymbol{t}^f$ is specified via the FSI formulation of choice. The traction and velocity terms on the interface Γ_{out} are given as a function of the solution $\boldsymbol{v}'$ in Ω'^f that can be approximated by momentum and mass operators $M=\{M_m, M_c\}^{\text{T}}|_{\Gamma_{\text{out}}}$ and $H=\{H_m, H_c\}^{\text{T}}|_{\Gamma_{\text{out}}}$ depending on the chosen model of the circulation in Ω'^f. We have:

$$\begin{aligned}&\int_{\Gamma_{\text{out}}}\{\boldsymbol{w}'\cdot(-p'\boldsymbol{I}+\boldsymbol{\tau}')-q'\boldsymbol{v}'\}\cdot\boldsymbol{n}'da=\\&\int_{\Gamma_{\text{out}}}\{\boldsymbol{w}'\cdot[M_m(\boldsymbol{v}',p')+H_m]-q'[M_c(\boldsymbol{v}',p')+H_c]\}\cdot\boldsymbol{n}'da=\\&-\int_{\Gamma_{\text{out}}}\{\boldsymbol{w}\cdot[M_m(\boldsymbol{v},p)+H_m]-q[M_c(\boldsymbol{v},p)+H_c]\}\cdot\boldsymbol{n}^f da\end{aligned}\tag{2}$$

A lumped-parameter model was used to represent the circulation in the downstream domain. Specifically, we adopted the standard three-component Windkessel model that requires the definition of a proximal resistance R_p, compliance C, and distal resistance R_d. Considering this, we have

$$-\int_{\Gamma_{\text{out}}}\boldsymbol{w}\cdot M_m(\boldsymbol{v},p)\cdot\boldsymbol{n}^f da=\int_{\Gamma_{\text{out}}}\boldsymbol{w}\cdot\boldsymbol{n}^f\left\{R_p\int_{\Gamma_{\text{out}}}\boldsymbol{v}\cdot\boldsymbol{n}^f da+\int_0^t\exp[-(t-t_1)/(R_dC)]\int_{\Gamma_{\text{out}}}\boldsymbol{v}(t_1)\cdot\boldsymbol{n}^f da dt_1\right\}da\tag{3}$$

$$-\int_{\Gamma_{\text{out}}}\boldsymbol{w}\cdot H_m\cdot\boldsymbol{n}^f da=\int_{\Gamma_{\text{out}}}\boldsymbol{w}\cdot n^f\left\{\left[p(0)-R_p\int_{\Gamma_{\text{out}}}\boldsymbol{v}(0)\cdot\boldsymbol{n}^f da\right]\exp[-t/(R_dC)]\right\}da\tag{4}$$

$$\begin{aligned}&\int_{\Gamma_{\text{out}}}qM_c(\boldsymbol{v},p)\cdot\boldsymbol{n}^f da=\int_{\Gamma_{\text{out}}}q\boldsymbol{v}\cdot\boldsymbol{n}^f da\\&\int_{\Gamma_{\text{out}}}qH_c\cdot\boldsymbol{n}^f da=0\end{aligned}\tag{5}$$

2.2.2. Method for Fluid-Structure Interaction—The coupled-momentum method for FSI was used to account for the deformability of the arterial network [11]. This method is appropriate for modeling wave propagation phenomena in large arterial networks due to the minimal additional computational effort that is required over the non-FSI, rigid wall formulation. This monolithic, fixed-mesh configuration method embeds the elasto-dynamics equations of the vessel wall into the variational form of the fluid problem via the definition of a fictitious body force driving the motion of the wall. By using a thin-wall membrane assumption, the fictitious body force is related to the traction $\boldsymbol{t}^f$ at the fluid-solid interface Γ_t, providing a closure for the term in equation (1):

$$\int_{\Gamma_t}\{-\boldsymbol{w}\cdot\boldsymbol{t}^f\}da=\int_{\Gamma_s}h\rho\boldsymbol{w}\cdot\dot{\boldsymbol{v}}\,dA+\int_{\Gamma_s}h\nabla\boldsymbol{w}:\mathscr{L}(\boldsymbol{P}_{\mathcal{K}_s})dA-\int_{\Gamma^s_{\text{out}}}h\boldsymbol{w}\cdot\boldsymbol{h}^s dL\tag{6}$$

where h and ρ are the vessel wall thickness and density, respectively, Γ_s represents the reference (average) configuration for the position of the arterial wall over the cardiac cycle, $\mathscr{L}(\boldsymbol{P}_{\mathcal{K}_s})$ is the linearization of the first Piola-Kirchhoff stress tensor, and Γ^s_{out} is a boundary

of the configuration Γ_s where a traction $\boldsymbol{h}^s$ is prescribed [10]. $\mathscr{L}(\boldsymbol{P}_{\kappa_*})$ may be obtained by linearization of a non-linear constitutive law via the theory of *Small on Large* [6] and will be used in subsequent works to assign experimentally-derived biaxial constitutive laws to the arterial wall [14]. In this present work, however, we used a simple analog of arterial stiffness given by a linear, isotropic constitutive model, characterized by the Young's modulus, E. In this case, $\mathscr{L}(\boldsymbol{P}_{\kappa_*}) = \tilde{\boldsymbol{K}}\tilde{\boldsymbol{\varepsilon}} + \tilde{\boldsymbol{P}}$, with

$$\tilde{\boldsymbol{K}} = \frac{E}{1-\nu^2}\begin{pmatrix} 1 & \nu & 0 & 0 & 0 \\ \nu & 1 & 0 & 0 & \\ 0 & 0 & 0.5(1-\nu) & 0 & 0 \\ 0 & 0 & 0 & 0.5k(1-\nu) & 0 \\ 0 & 0 & 0 & 0 & 0.5k(1-\nu) \end{pmatrix} \quad (7)$$

$$\tilde{\boldsymbol{\varepsilon}} = \begin{pmatrix} \partial u_1/\partial x_1 \\ \partial u_2/\partial x_2 \\ \partial u_1/\partial x_2 + \partial u_2/\partial x_1 \\ \partial u_3/\partial x_1 \\ \partial u_3/\partial x_2 \end{pmatrix}, \quad \tilde{\boldsymbol{P}} = \begin{pmatrix} P_{11} \\ P_{22} \\ P_{12} \\ P_{31} \\ P_{32} \end{pmatrix} \quad (8)$$

where ν represents the Poisson's ratio, k is a transverse shear factor, $\boldsymbol{u}$ is the displacement vector, and $\tilde{\boldsymbol{P}}$ is a pre-stress tensor.

2.2.3. Model for Perivascular Tissue Support—To obtain physiologically realistic vessel wall dynamics, it is necessary to account for the mechanical forces exerted by the perivascular tissues and other organs on the arterial walls. Indeed, the major arteries of the body are tethered to the surrounding tissue as opposed to being suspended in space. We thus apply a simple traction boundary condition on the vessel wall boundary to represent the mechanical behavior of the perivascular tissue [24] and to stabilize potential nonphysiological oscillations in the movement of the unsupported arterial wall. This traction boundary condition mimics the effect of a viscoelastic foundation and is added to equation (1) via the following integral term:

$$-\int_{\Gamma_t} \boldsymbol{w} \cdot (k_s \boldsymbol{u} + c_s \boldsymbol{v}) dA \quad (9)$$

Here, the parameters k_s and c_s control the stiffness and damping behavior, respectively.

2.3. Parameter Specification

2.3.1. Arterial Wall Material Properties—The manually generated centerline paths and 2-D segmentations obtained in the geometric reconstruction process were used to assign non-uniform distributions of vessel wall stiffness (i.e. E) and thickness h according to the following procedure: We first determined an equivalent radius r for each of the segmentations along the centerline path. Since each 2-D segmentation is not necessarily circular, the equivalent radius is simply obtained from the area of the segmented region. The local thickness at the segmentation was then defined as ten percent of r [26]. The distribution of E was assigned by first using an empirical formula derived by Reymond et al. [33] from measurements relating pulse wave velocity (PWV) to vessel radius: PWV = $\alpha/(2r)^{\beta}$, where $\alpha = 13.3$ and $\beta = 0.3$. Here, r is given in mm and PWV in m/s. Then, using the Moens-Korteweg formula we arrived at the following expression for E (given in MPa) as a function of the local radius:

$$E(\text{MPa}) = 0.001 \frac{\rho}{h} \frac{\alpha^2}{(2r)^{2\beta-1}} \quad (10)$$

where ρ and h are given in [cgs] units. The values of E and h at the segmentation locations were interpolated linearly along the centerline and then projected on to the vessel wall by finding the shortest distance from each surface triangle to the centerline (see Figure 3).

2.3.2. Outflow Boundary Condition Parameters—The resistance of each outlet, which is the sum of the proximal and distal resistances ($R_p + R_d$) was adjusted in an iterative manner so that the predicted flow distributions in each vascular region were within 3% of reported values [46]. We defined a "total equivalent peripheral resistance", R_T, for each color-coded vascular region (see Tables 1 and 2) where $R_T = (\Sigma_i 1/R_i)^{-1}$ and R_i is the individual outlet resistance ($R_p + R_d$). R_i were computed using the relation: $R_T/R_i = A_i/A_T$ where A_i is the cross-sectional area of the individual outlet and A_T is the total cross-sectional area of the outlets in a vascular region. For each region, R_T was adjusted to achieve the desired regional flow. Similarly, we defined a "total equivalent peripheral compliance," $C_T = (\Sigma_i C_i)$, and computed the individual C_i using the relation: $C_i/C_T = A_i/A_T$. Thus, we assumed that in each vascular region the amount of flow and the peripheral compliance at each outlet are proportional to its area. We assumed that the ratio of the proximal to total resistance, $R_p/(R_p + R_d)$, is 0.056 [17], except for the outlets where no reverse flow was expected. In such outlets (i.e., renals and cerebral vessels), we arbitrarily assumed this ratio varied between 0.1 and 0.2.

3. Results

3.1. Trunk model: Baseline Conditions

As a precursor to the full-body simulation, we first focused on a subset of the full-body geometry encompassing the vessels inferior to the carotids and superior to the femoral arteries. This trunk model (see Figure 4), due to its smaller size, facilitated the process of tuning the outflow boundary conditions and the distribution of arterial wall stiffness. The Windkessel parameters used in this model are reported in Table 1. The vessel wall density was $\rho = 1.06\ g/cm^3$, the Poisson's ratio $\nu = 0.5$, and the transverse shear factor $k = 0.833$. We considered a distribution of stiffness representative of a younger subject by scaling equation (10) by a factor of 0.4 (see Figure 5). We prescribed a representative ascending aortic flow waveform (see Figure 7) with an average cardiac output of 5 L/min and a heart rate of 60 beats per second. The finite element mesh consisted of 1,721,395 linear tetrahedra and 368,170 nodes. We used a time step size of 0.1 ms and ran the simulation for three cardiac cycles to achieve cycle-to-cycle periodicity in the results. Figure 5 shows peak systolic maps for the wall shear stress and volume rendering of the velocity magnitude. Figure 6 demonstrates good agreement between simulated regional flow distributions and reported values in the literature [46], which were scaled to accommodate the absence of coronary and intercostal arteries in the model.

Cross-sectional flow and pressure waveforms at multiple sites in the model (see Figure 7) exhibit realistic qualitative characteristics; namely, a physiologically relevant range for flow and pressure at each outlet, reverse flow in the abdominal aorta during diastole, and forward flow throughout the cycle in the renal arteries [26]. Pressure waveforms are shown at six sites along the aorta and into the left common iliac artery (Figure 8). Pressures ranged from 104/81 mmHg in the ascending aorta to 119/76 mmHg in the common iliac artery. The pressure wave exhibited a large increase in amplitude as it traveled down the aorta. Such pressure amplification is well known to occur most prominently in younger healthy subjects. Pulse wave velocity (PWV) values were obtained by measuring the centerline distance

between measurement sites and the time elapsed between the "feet" of the corresponding pressure waves [7]. Figure 8 further shows an increase in PWV down the aorta. This is in good qualitative agreement with experimental measurements of wave speed. PWV is smallest in the ascending aorta (3.01 m/s), where the vessel wall is the most compliant, and reaches a maximum value in the stiffer abdominal aorta (4.30 m/s) before declining again at the iliac bifurcation level.

3.2. Trunk Model: Age-related Stiffening, Hypertension and Pressure Pulse Propagation

We next investigated the impact of temporal changes in wall mechanical properties on pressure pulse propagation. To this end, we performed two additional simulations in which arterial stiffness was increased to represent age-related changes in mechanical properties (see Figure 9). These two additional cases, labeled "middle-aged" and "elderly", were obtained by scaling equation (10) by a factor of 0.8 and 1.2, respectively. This uniformly multiplied the stiffness of the baseline "young" case by a factor of two and three. Figure 9 shows pressure waveforms at six sites in the aorta for all three cases. Numerical values for the pulse pressure (the difference between systolic and diastolic pressures) and amplification factor, defined as the ratio of the local pulse pressure to the pulse pressure at site 1, are provided for each waveform. Results show that pulse pressure increased with increasing stiffness at every site. However, the amplification factor between sites 1 and 6 decreases with increased stiffness, ranging from 1.88 in the "young" case to 1.13 in the "elderly" case. This is in agreement with experimental findings that report a decrease in pressure amplification with age [26]. Lastly, the table at the bottom of Figure 9 compares PWV amongst the three cases. As expected, PWV increased with increased levels of arterial stiffness. These changes were not spatially uniform: the ascending aorta experienced the smallest increase in PWV (from 3.01 m/s in the "young" case to 3.57 m/s in the "elderly" case) whereas the abdominal aorta experienced the largest increase (from 4.30 m/s to 8.00 m/s). The "aortic-to-iliac" PWV between locations 1 and 6, analogous to the CF-PWV, increased as the aorta stiffened.

3.3. Full Body Model

The full body model contains the primary large arteries of the human vasculature from head to foot. Figure 10 shows the 82 outlets of the model, grouped together and colored-coded by perfusion region. Closeup views depict the cerebral vasculature (A), subclavian branches (B), arm arteries (C, D), mesenteric branches (E), branches from the celiac trunk and the renal arteries (F), and the major leg arteries and their branches (I-N). All outflow vessels are labeled with unique identifiers. The Windkessel parameters used in this model are reported in Table 2. The vessel wall density was $\rho = 1.06\ g/cm^3$, the Poisson's ratio $\nu = 0.5$, and the transverse shear factor $k = 0.833$. The distribution of mechanical wall properties was obtained by scaling equation (10) by a factor of 1.2; therefore the full body model has a similar level of arterial stiffness as the "elderly" trunk model. We prescribed the same ascending aortic flow waveform as in the trunk model. The finite element mesh consisted of 14,438,720 linear tetrahedra and 2,674,545 nodes. We used a time step size of 0.05 ms and ran the simulation for three cardiac cycles to achieve cycle-to-cycle periodicity in the results. The run time was approximately 48 hours per cardiac cycle using 384 cores of a cluster containing AMD Barcelona processors (Ranger at Texas Advanced Computing Center). Figure 12 displays color maps of wall stiffness, peak systolic wall shear stress and a volume rendering of velocity magnitude for this model.

Figure 11 shows cross-sectional flow and pressure waveforms at multiple sites in the model. Reverse flow is mostly absent in the descending thoracic aorta, but develops in the infra-renal region of the abdominal aorta and is also seen in the iliac and femoral arteries. Forward flow is observed throughout the cardiac cycle in the renal arteries, common carotid arteries,

and middle cerebral arteries. Flow waves in the subclavian and brachial arteries show a sharp systolic peak followed by a secondary peak. In particular, the shape of the brachial flow wave shows agreement with experimental measurements [12]. Pressures ranged from 151/81 mmHg in the ascending aorta to 163/73 mmHg in the tibial artery. Time-averaged mean pressure dropped from 114 mmHg in the ascending aorta to 104 mmHg in the tibial artery. The ratio of the tibial pulse pressure to ascending aortic pulse pressure was 1.30. The table in Figure 11 shows PWV between individual sites down the aorta and the arteries of the left leg. The carotid-to-femoral pulse wave velocity (CF-PWV), computed from pressure waves at the right common carotid artery and the femoral artery was 8.81 m/s.

4. Discussion

In this article, we presented an analysis of unsteady three-dimensional hemodynamics within two deformable arterial models: one containing the main arteries in the trunk region and the other containing the main arteries of the entire body from head to foot. Due to the complexity of these models, the following methodologies were required to produce a physiologically realistic solution: a coupled-momentum method for fluid-structure-interaction, a multi-domain method for outflow boundary condition specification, an external tissue support boundary condition for representing perivascular tethering, and a method for field-driven mesh adaptation. While these individual methodological approaches have been previously published, this is the first combination of these separate methods to build a model at the full-body scale. The simulations resulted in physiologically realistic pressure and flow waveforms as well as realistic spatial variations in pulse wave velocity. Furthermore, and consistent with the literature on arterial aging, the trunk model showed that increased arterial stiffness resulted in a reduction of pressure wave amplification and increased PWV values. In the following paragraphs, we discuss a few aspects regarding the adopted methodological approach and the validity of the simulation results.

4.1. Multi-Scale vs. Multi-Resolution

The coupled multi-domain method for outflow boundary condition specification is a variational multi-scale formulation that facilitates the coupling of different spatial scales modeled in the upstream and downstream domains. The Navier-Stokes equations are used to characterize 3-D blood flow in the large arteries at the continuum scale in the upstream domain, whereas reduced-order models (in this case, zero-dimensional lumped-parameter Windkessel models) are used to represent flow in the microcirculation (i.e., downstream domain). While multiple spatial scales are not simultaneously considered within each individual domain, the overall model is “multi-scale” since it accounts for the impact that flow in the microcirculation has on the macrocirculation. However, one could also interpret this approach as a “multi-resolution” method, since different parts of the domain are modeled using different levels of spatial resolution (3-D vs 0-D).

4.2. FSI Solution Strategy

The coupled-momentum method for fluid-structure interaction assumes linearized kinematics and constitutive behavior and is thus most appropriate when the arterial wall deformations are small, as is the case for the majority of vessels in the full-body arterial network. This method has been shown to be highly scalable [49] and to have a small additional computational cost compared to that of rigid-wall formulations [11]. There are of course a number of other methods for cardiovascular fluid-structure-interaction: extensive work has been done in developing moving-domain formulations such as arbitrary-Lagrangian-Eulerian (ALE) methods [30, 13, 24, 39, 8] that can accommodate large deformations of the vessel wall. Although using an ALE method would allow us to accurately capture the motion of the ascending aorta, the computational cost would be

currently prohibitive for models of the scale presented in this paper. A hybrid strategy whereby an ALE method is used in certain regions and the linear fixed-mesh coupled momentum formulation is used elsewhere could provide the best of both worlds.

4.3. Arterial Stiffening and Wave Propagation

Arterial stiffening due to normal aging or disease results in increased PWV values in the central arteries. An important consequence of increased stiffness is that reflected pressure waves from the peripheral circulation arrive earlier at the ascending aorta and constructively interfere with the incident waves, resulting in an "augmented" pressure waveform [26, 7]. The augmentation index (AIx) is a metric that quantifies the increase in pulse pressure due to wave reflection and is commonly used as a surrogate for arterial stiffness. However, the determination of AIx requires identifying a "shoulder" on the rising limb of the pressure wave during systole. This feature is not always identifiable, and indeed, it was not clearly seen in the simulation results. On the other hand, pressure amplification, which is simply a ratio between peripheral pulse pressure and aortic pulse pressure (and thus inversely related to AIx), can be measured more accurately and is therefore an alternative indicator of arterial stiffness [1]. In the arterial stiffening analysis, it was apparent that increased stiffness altered the timing of the reflected pressure waves arriving at the ascending aorta. Specifically, whereas in the "young" case two peaks in the pressure waveform were clearly visible (the late second peak corresponds to a reflected wave from the periphery), in the "elderly" case there is a single peak (see location 1 in Figure 9) of larger magnitude, due to the earlier arrival of the reflected waves at the ascending aorta.

4.4. Wave Propagation in the Full-Body model

The distribution of wall stiffness in the full-body model is comparable to that of the "elderly" trunk case, and the aortic pulse pressures (70–80 mmHg) and pressure waveforms in the two models are comparable. PWV increased moving from the ascending to the descending aorta due to anatomical tapering and increasing arterial stiffness, but decreased after the aortic bifurcation, as shown in Figure 11. These results are in line with the study published by Latham et al. [18], in which aortic PWV was measured in human subjects using a catheter with six manometers. Their findings showed a marked increase in PWV moving down the aorta and a reduction in PWV after the aortic bifurcation.

4.5. Three-Dimensional Models vs. One-Dimensional Models

1-D models of wave propagation have been used extensively to investigate hemodynamics in the human arterial tree. These models describe spatially-averaged quantities of pressure and flow in the axial direction and therefore contain far fewer degrees-of-freedom in comparison to a 3-D model ($O(10^3)$ in 1-D versus $O(10^6)$ in 3-D). Therefore, the required computational cost of 1-D formulations is modest: an analysis of wave propagation in the arterial tree can be produced within a clinically-relevant time frame using a laptop computer.

In contrast, 3-D analysis requires substantial computational resources. Parallel computing using a large number of processors is needed to produce results in a clinically-relevant time frame. Of course, the advantage of 3-D formulations is the ability to account for important anatomical features such as curvature, bifurcations, sudden changes in cross-sectional area and circumferentially-varying wall properties. None of these anatomical considerations can be directly addressed in a 1-D setting. We thus emphasize that 3-D models avoid the limitations of 1-D models while producing the same quantities, i.e. spatially-averaged pressure and flow directly extracted from the 3-D velocity and pressure fields as illustrated in the results above. The availability of the full 3-D velocity field (see Figure 12) enables further examination of flow features and wall shear maps. Taking advantage of both 1-D and

3-D approaches, an efficient modeling strategy would involve using 1-D models to quickly estimate inflow and outflow boundary conditions for the 3-D model.

4.6. Limitations and Future Work

The task of assigning parameters for outflow boundary conditions and vessel wall material properties in a subject-specific manner is nontrivial. Ideally, non-invasive clinical measurements would be used to tune the model parameters. However, these measurements usually provide partial information on the velocity field, such as flow waveforms at discrete locations. Regarding the pressure, time-resolved non-invasive data can only be obtained for superficial vessels using applanation tonometry and central pressure must be estimated indirectly via transfer functions. Furthermore, certain tissue properties such as the internal stress cannot be measured non-invasively. Experimental ex-vivo techniques have enabled the characterization of biaxial non-linear material properties for the vessel wall by providing adequate longitudinal stretching and pressure-perfusion to the specimen [14]. In subsequent works, the task of boundary and material parameter specification can be improved by using advanced time-resolved volumetric imaging techniques such as 4D-PC MRI that provide velocity data in the entire volume of interest [20]. Furthermore, recently developed methods for cardiovascular data assimilation [23] could be used to estimate model parameters from time-resolved images of wall motion and non-invasive measurements of flow and pressure.

In this paper we computed the outflow boundary condition parameters for both the trunk and full-body models in an ad-hoc manner, using the method described in section 2.3.2. This resulted in several Windkessel coefficients in the common outlets to both models (i.e., the arm and leg regions) to be different, even though the total equivalent peripheral resistance and compliance (R_T and C_T respectively) of these regions were identical. In subsequent works, a more systematic approach could be adopted to ensure consistency in boundary condition parameters between a full-body scale model and an arbitrarily truncated model.

The resolution of the meshes presented here is insufficient to reach grid independence in the wall shear stress fields [19]; results in Figure 12 are thus provided simply to illustrate ultimate capability. Indeed, the goal of this current work was to characterize global wave propagation phenomena and to demonstrate the feasibility of a 3-D framework for calculating hemodynamics in full-body scale anatomical models. In subsequent works, a two-step approach for accurately resolving wall shear in localized regions could be adopted. In such an approach, a full body model with a moderate level of mesh resolution could provide the boundary conditions for a truncated, more finely discretized model.

The full-body model presented here does not include the main coronary arteries and the intercostal arteries. These branches carry a significant portion of the cardiac output and, in the case of the intercostals, might impact wave propagation in the aorta. The inclusion of the coronaries will be useful to investigate the impact of arterial stiffening on coronary blood flow.

A further limitation of the current model is the use of a prescribed flow waveform at the inlet. A lumped-parameter heart model [15] can be used to simulate the coupling between the left ventricle and the arterial network, This approach will allow us to investigate the effect of increased arterial stiffening on the workload of the heart.

In the age-related stiffening study we simply modified the values of the arterial stiffness in going for the baseline “young” case to the “middle-aged” and “elderly” cases, and assumed no changes in the anatomy. It is well-known however that the aorta becomes more tortuous with aging, due to the loss of longitudinal tethering and decrease in height of the individual.

A more rigorous study on arterial aging hemodynamics would include not only changes in mechanical properties but also different arterial geometries for subjects of different ages.

Finally, validation is a crucial step for any modeling task. There have been several studies that include validation for 1-D models using in vitro and subject-specific in vivo measurements of flow and pressure [3, 32, 33]. The 3-D models presented in this work must be validated in the same manner. Furthermore, a comparison between 1-D and 3-D modeling approaches in full-body arterial networks is necessary to assess the differences in overall hemodynamics between the two formulations.

4.7. Clinical Implications

Diverse clinically measurable metrics - pulse wave velocity, pulse pressure, augmentation index, arterial distensibility, and so forth - have found considerable clinical acceptance as indicators of cardiovascular function and predictors of cardiovascular risk [22, 9, 25, 5]. For example, it has been shown empirically that the CF-PWV correlates very well with both risk and disease [22], leading some to refer to CF-PWV as the “gold standard” of measurement of arterial stiffness [25] and the NIH to concur that it is a “direct measure of arterial stiffness” (RFA-HL-10-027). We emphasize, however, that CF-PWV is simply a convenient clinical metric that reflects an underlying spatially-averaged structural stiffness of a tapering arterial tree from the carotids to the femorals. There is a need to understand the CF-PWV better from the perspective of mechanics as well as from the perspective of clinical implications. Indeed, notwithstanding the increased clinical acceptance of CF-PWV as a metric of changes in arterial stiffness, McEniery et al. suggested that “augmentation index might be a more sensitive marker of arterial stiffening and risk in younger individuals (< 50 years of age) but aortic PWV is likely to be a better measure in older individuals (> 50 years of age) [21]”, that is, only after marked and diffuse changes in stiffness have occurred. Lakatta et al. wrote further that “Evaluation of the diastolic decay of pulse wave contour may provide insights into the characteristics and pathology of more distal vessels in which reflected waves originate [16].” Wang et al. similarly suggested that “Although aortic stiffness indexed by carotid-femoral PWV is the gold standard measurement for arterial stiffness, measurement of the intensity of wave reflection is also relevant to identify subjects with early vascular aging… [42]”

Based on empirical findings, therefore, there is a pressing need to investigate more deeply the utility of the many candidate clinical metrics of arterial aging as well as their potential in reflecting the underlying structural mechanisms that lead to adverse cardiovascular diseases. We submit that, via well designed parametric studies, computational models offer considerable promise in contributing to this goal. In particular, there is a need to investigate the hypothesis that increased arterial stiffening likely initiates in more proximal large arteries, then propagates to more distal large arteries and eventually to the microvessels. Modeling studies can facilitate the delineation of effects of spatially and temporally progressive increases in large artery stiffening on system-level hemodynamics, with the potential to identify improved indicators of early stiffening that may allow an earlier clinical intervention that can prevent the longer-term irreversible changes to the microstructure that otherwise inevitably occur.

Acknowledgments

This work was supported by the United States National Institutes of Health (NIH) grant R01 HL-105297. The simulations were supported in part by a United States National Science Foundation (NSF) Grant CNS-0619926 and by a NSF Extreme Science and Engineering Digital Environment (XSEDE) startup allocation. The authors acknowledge financial support from the United Kingdom Department of Health via the National Institute for Health Research (NIHR) comprehensive Biomedical Research Centre award to Guy’s & St Thomas’ NHS Foundation Trust in partnership with King’s College London and King’s College Hospital NHS Foundation Trust.

References

1. Adji A, O'Rourke MF, Namasivayam M. Arterial stiffness, its assessment, prognostic value, and implications for treatment. American journal of hypertension. Jan; 2011 24(1):5–17. [PubMed: 20940710]
2. Agabiti-Rosei E, Mancia G, O'Rourke MF, Roman MJ, Safar ME, Smulyan H, Wang J-G, Wilkinson IB, Williams B, Vlachopoulos C. Central blood pressure measurements and antihypertensive therapy: a consensus document. Hypertension. Jul; 2007 50(1):154–160. [PubMed: 17562972]
3. Alastruey J, Khir AW, Matthys KS, Segers P, Sherwin SJ, Verdonck PR, Parker KH, Peiró J. Pulse wave propagation in a model human arterial network: Assessment of 1-D visco-elastic simulations against in vitro measurements. Journal of biomechanics. Aug; 2011 44(12):2250–2258. [PubMed: 21724188]
4. Avolio AP. Multi-branched model of the human arterial system. Medical & biological engineering & computing. Dec; 1980 18(6):709–718. [PubMed: 7230917]
5. Avolio AP, Van Bortel LM, Boutouyrie P, Cockcroft JR, McEniery CM, Protogerou AD, Roman MJ, Safar ME, Segers P, Smulyan H. Role of pulse pressure amplification in arterial hypertension: experts' opinion and review of the data. Hypertension. Aug; 2009 54(2):375–383. [PubMed: 19564542]
6. Baek S, Gleason RL, Rajagopal KR, Humphrey JD. Theory of small on large: Potential utility in computations of fluidGsolid interactions in arteries. Computer Methods in Applied Mechanics and Engineering. Jun; 2007 196(31–32):3070–3078.
7. Barodka VM, Joshi BL, Berkowitz DE, Hogue CW, Nyhan D. Review article: implications of vascular aging. Anesthesia and analgesia. May; 2011 112(5):1048–1060. [PubMed: 21474663]
8. Bazilevs Y, Calo VM, Zhang Y, Hughes TJR. Isogeometric FluidGstructure Interaction Analysis with Applications to Arterial Blood Flow. Computational Mechanics. Jun; 2006 38(4–5):310–322.
9. Boutouyrie P, Laurent S, Briet M. Importance of arterial stiffness as cardiovascular risk factor for future development of new type of drugs. Fundamental & clinical pharmacology. Jun; 2008 22(3): 241–246. [PubMed: 18485143]
10. Figueroa CA, Baek S, Taylor CA, Humphrey JD. A computational framework for fluid-solid-growth modeling in cardiovascular simulations. Computer Methods in Applied Mechanics and Engineering. 2009; 198(45–46):3583–3602. [PubMed: 20160923]
11. Figueroa CA, Vignon-Clementel IE, Jansen KE, Hughes TJR, Taylor CA. A coupled momentum method for modeling blood flow in three-dimensional deformable arteries. Computer Methods in Applied Mechanics and Engineering. 2006; 195(41–43):5685–5706.
12. Gault JH, Ross JR, Mason DT. Patterns of brachial arterial blood flow in conscious human subjects with and without cardiac dysfunction. Circulation. 1966:833–848. [PubMed: 5923846]
13. Gerbeau J-F, Vidrascu M, Frey P. Fluid-structure interaction in blood flows on geometries based on medical imaging. Computers & Structures. Jan; 2005 83(2–3):155–165.
14. Gleason RL, Gray SP, Wilson E, Humphrey JD. A multiaxial computer-controlled organ culture and biomechanical device for mouse carotid arteries. Journal of Biomechanical Engineering. 2004; 126(6):787–795. [PubMed: 15796337]
15. Kim HJ, Vignon-Clementel IE, Figueroa Ca, LaDisa JF, Jansen KE, Feinstein JA, Taylor CA. On coupling a lumped parameter heart model and a three-dimensional finite element aorta model. Annals of biomedical engineering. Nov; 2009 37(11):2153–2169. [PubMed: 19609676]
16. Lakatta EG, Wang M, Najjar SS. Arterial aging and subclinical arterial disease are fundamentally intertwined at macroscopic and molecular levels. Medical Clinics of North America. 2009; 93(3): 583–604. [PubMed: 19427493]
17. Laskey WK, Parker HG, Ferrari VA, Kussmaul WG, Noordergraaf A. Estimation of total systemic arterial compliance in humans. Journal of applied physiology (Bethesda, Md: 1985). Jul; 1990 69(1):112–119.
18. Latham RD, Westerhof N, Sipkema P, Rubal BJ, Reuderink P, Murgo JP. Regional wave travel and reflections along the human aorta: a study with six simultaneous micromanometric pressures. Circulation. 1985; 72(6):1257–1269. [PubMed: 4064270]

19. Les AS, Shadden SC, Figueroa CA, Park JM, Tedesco MM, Herfkens RJ, Dalman RL, Taylor CA. Quantification of hemodynamics in abdominal aortic aneurysms during rest and exercise using magnetic resonance imaging and computational fluid dynamics. Annals of biomedical engineering. Apr; 2010 38(4):1288–1313. [PubMed: 20143263]
20. Markl M, Draney MT, Hope MD, Levin JM, Chan FP, Alley MT, Pelc NJ, Herfkens RJ. Time-Resolved 3-Dimensional Velocity Mapping in the Thoracic Aorta. Journal of Computer Assisted Tomography. 2004; 28(4):459–468. [PubMed: 15232376]
21. McEniery CM, Yasmin, Hall IR, Qasem A, Wilkinson IB, Cockcroft JR. Normal vascular aging: differential effects on wave reflection and aortic pulse wave velocity: the Anglo-Cardiff Collaborative Trial (ACCT). Journal of the American College of Cardiology. 2005; 46(9):1753–1760. [PubMed: 16256881]
22. McEniery CM, Yasmin, Maki-Petaja KM, McDonnell BJ, Munnery M, Hickson SS, Franklin SS, Cockcroft JR, Wilkinson IB. The impact of cardiovascular risk factors on aortic stiffness and wave reflections depends on age: the Anglo-Cardiff Collaborative Trial (ACCT III). Hypertension. Oct; 2010 56(4):591–597. [PubMed: 20696989]
23. Moireau P, Bertoglio C, Xiao N, Figueroa Ca, Taylor Ca, Chapelle D, Gerbeau J-F. Sequential identification of boundary support parameters in a fluid-structure vascular model using patient image data. Biomechanics and modeling in mechanobiology. Jul.2012
24. Moireau P, Xiao N, Astorino M, Figueroa CA, Chapelle D, Taylor CA, Gerbeau J-F. External tissue support and fluid-structure simulation in blood flows. Biomechanics and modeling in mechanobiology. Feb; 2011 11(1–2):1–18. [PubMed: 21308393]
25. Najjar SS, Scuteri A, Shetty V, Wright JG, Muller DC, Fleg JL, Spurgeon HP, Ferrucci L, Lakatta EG. Pulse wave velocity is an independent predictor of the longitudinal increase in systolic blood pressure and of incident hypertension in the Baltimore Longitudinal Study of Aging. Journal of the American College of Cardiology. Apr; 2008 51(14):1377–1383. [PubMed: 18387440]
26. Nichols, WW.; O'Rourke, MF. McDonald's blood flow in arteries: theoretical, experimental, and clinical principles. Arnold, Hodder, editor. Vol. 11. Distributed in the United States of America by Oxford University Press; 1998.
27. Nilsson PM, Boutouyrie P, Laurent S. Vascular aging: A tale of EVA and ADAM in cardiovascular risk assessment and prevention. Hypertension. Jul; 2009 54(1):3–10. [PubMed: 19487587]
28. Olufsen MS. Structured tree outflow condition for blood flow in larger systemic arteries. American journal of physiology-Heart and circulatory physiology. 1999; 276(1):H257–H268.
29. O'Rourke MF, Hashimoto J. Mechanical factors in arterial aging: a clinical perspective. Journal of the American College of Cardiology. Jul; 2007 50(1):1–13. [PubMed: 17601538]
30. Perktold K, Rappitsch G. Computer simulation of local blood flow and vessel mechanics in a compliant carotid artery bifurcation model. Journal of biomechanics. Jul; 1995 28(7):845–856. [PubMed: 7657682]
31. Redheuil A, Yu W-C, Wu CO, Mousseaux E, de Cesare A, Yan R, Kachenoura N, Bluemke D, Lima JAC. Reduced ascending aortic strain and distensibility: earliest manifestations of vascular aging in humans. Hypertension. Feb; 2010 55(2):319–326. [PubMed: 20065154]
32. Reymond P, Bohraus Y, Perren F, Lazeyras F, Stergiopulos N. Validation of a patient-specific one-dimensional model of the systemic arterial tree. American journal of physiology Heart and circulatory physiology. 2011; 301(3):H1173–82. [PubMed: 21622820]
33. Reymond P, Merenda F, Perren F, Rüfenacht D, Stergiopulos N. Validation of a one-dimensional model of the systemic arterial tree. American journal of physiology. Heart and circulatory physiology. Jul; 2009 297(1):H208–22. [PubMed: 19429832]
34. Safar ME. Arterial aging–hemodynamic changes and therapeutic options. Nature reviews. Cardiology. Aug; 2010 7(8):442–449.
35. Sahni O, Muller J, Jansen KE, Shephard MS, Taylor CA. Efficient anisotropic adaptive discretization of the cardiovascular system. Computer Methods in Applied Mechanics and Engineering. Aug; 2006 195(41–43):5634–5655.

36. Schaaf BW, Abbrecht PH. Digital computer simulation of human systemic arterial pulse wave transmission: a nonlinear model. Journal of Biomechanics. 1972; 5(4):345–364. [PubMed: 4666197]
37. Sherwin SJ, Franke V, Peiro J, Parker KH. One-dimensional modelling of a vascular network in space-time variables. Journal of Engineering Mathematics. Dec; 2003 47(3):217–250.
38. Stergiopulos N, Young DF, Rogge TR. Computer simulation of arterial flow with applications to arterial and aortic stenoses. Journal of biomechanics. Dec; 1992 25(12):1477–1488. [PubMed: 1491023]
39. Torii R, Oshima M, Kobayashi T, Takagi K, Tezduyar TE. FluidGstructure Interaction Modeling of Aneurysmal Conditions with High and Normal Blood Pressures. Computational Mechanics. May; 2006 38(4–5):482–490.
40. Vignon-Clementel IE, Figueroa CA, Jansen KE, Taylor CA. Outflow boundary conditions for three-dimensional finite element modeling of blood flow and pressure in arteries. Computer Methods in Applied Mechanics and Engineering. 2006; 195(29–32):3776–3796.
41. Vignon-Clementel IE, Figueroa CA, Jansen KE, Taylor CA. Outflow boundary conditions for 3D simulations of non-periodic blood flow and pressure fields in deformable arteries. Computer methods in biomechanics and biomedical engineering. Oct; 2010 13(5):625–640. [PubMed: 20140798]
42. Wang K-L, Cheng H-M, Sung S-H, Chuang S-Y, Li C-H, Spurgeon HA, Ting C-T, Najjar SS, Lakatta EG, Yin FCP, Chou P, Chen C-H. Wave reflection and arterial sti3ness in the prediction of 15-year all-cause and cardiovascular mortalities: a community-based study. Hypertension. Mar; 2010 55(3):799–805. [PubMed: 20065155]
43. Westerhof BE, Guelen I, Stok WJ, Lasance HAJ, Ascoop CAPL, Wesseling KH, Westerhof N, Bos WJW, Stergiopulos N, Spaan JAE. Individualization of transfer function in estimation of central aortic pressure from the peripheral pulse is not required in patients at rest. Journal of applied physiology (Bethesda, Md: 1985). Dec; 2008 105(6):1858–1863.
44. Westerhof N, Bosman F, de Vries CJ, Noordergraaf A. Analog studies of the human systemic arterial tree. Journal of biomechanics. 1969; 2(2):121–143. [PubMed: 16335097]
45. Whiting CH, Jansen KE. A stabilized finite element method for the incompressible Navier-Stokes equations using a hierarchical basis. International Journal for Numerical Methods in Fluids. Jan; 2001 35(1):93–116.
46. Williams LR, Leggett RW. Reference values for resting blood flow to organs of man. Clinical Physics and Physiological. 1989; 10(3):187–217.
47. Wilson JS, Baek S, Humphrey JD. Importance of initial aortic properties on the evolving regional anisotropy, stiffness and wall thickness of human abdominal aortic aneurysms. Journal of the Royal Society, Interface/the Royal Society. Apr.2012
48. Wilson, N.; Wang, K.; Dutton, R.; Taylor, CA. Medical Image Computing and Computer-Assisted Intervention GMICCAI 2001. Springer; 2001. A software framework for creating patient specific geometric models from medical imaging data for simulation based medical planning of vascular surgery; p. 449-456.
49. Zhou M, Sahni O, Kim HJ, Figueroa CA, Taylor CA, Shephard MS, Jansen KE. Cardiovascular flow simulation at extreme scale. Computational Mechanics. Dec; 2009 46(1):71–82.

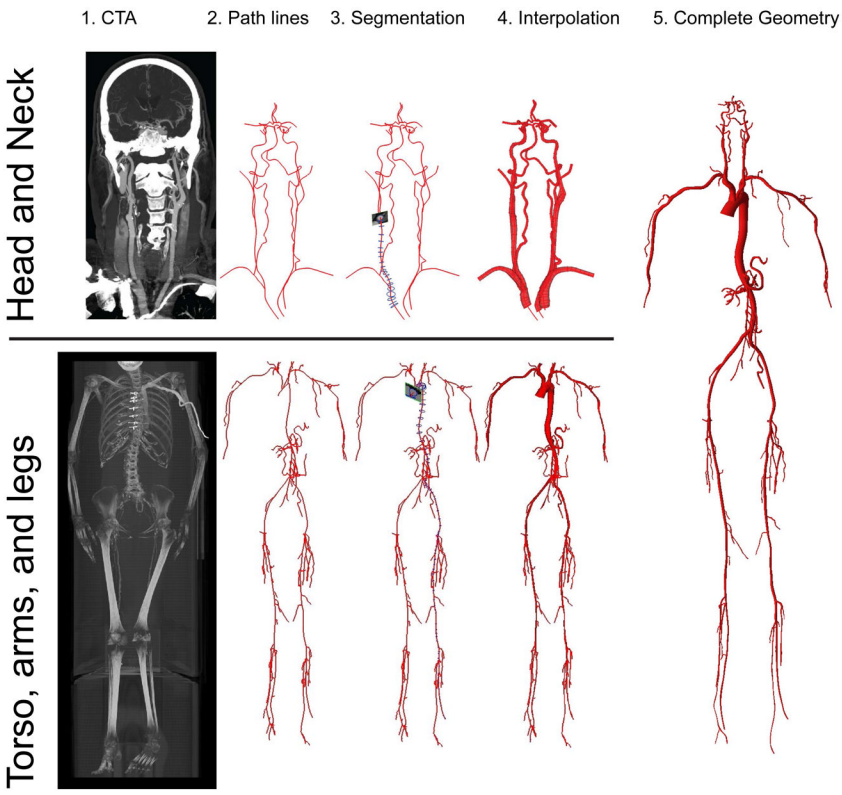

Figure 1.
The arterial geometry was reconstructed separately for the head/neck and the rest of the body using CT image data from two subjects. Segmentations performed along manually selected path lines were interpolated to produce a 3-D geometric solid model of each vessel.

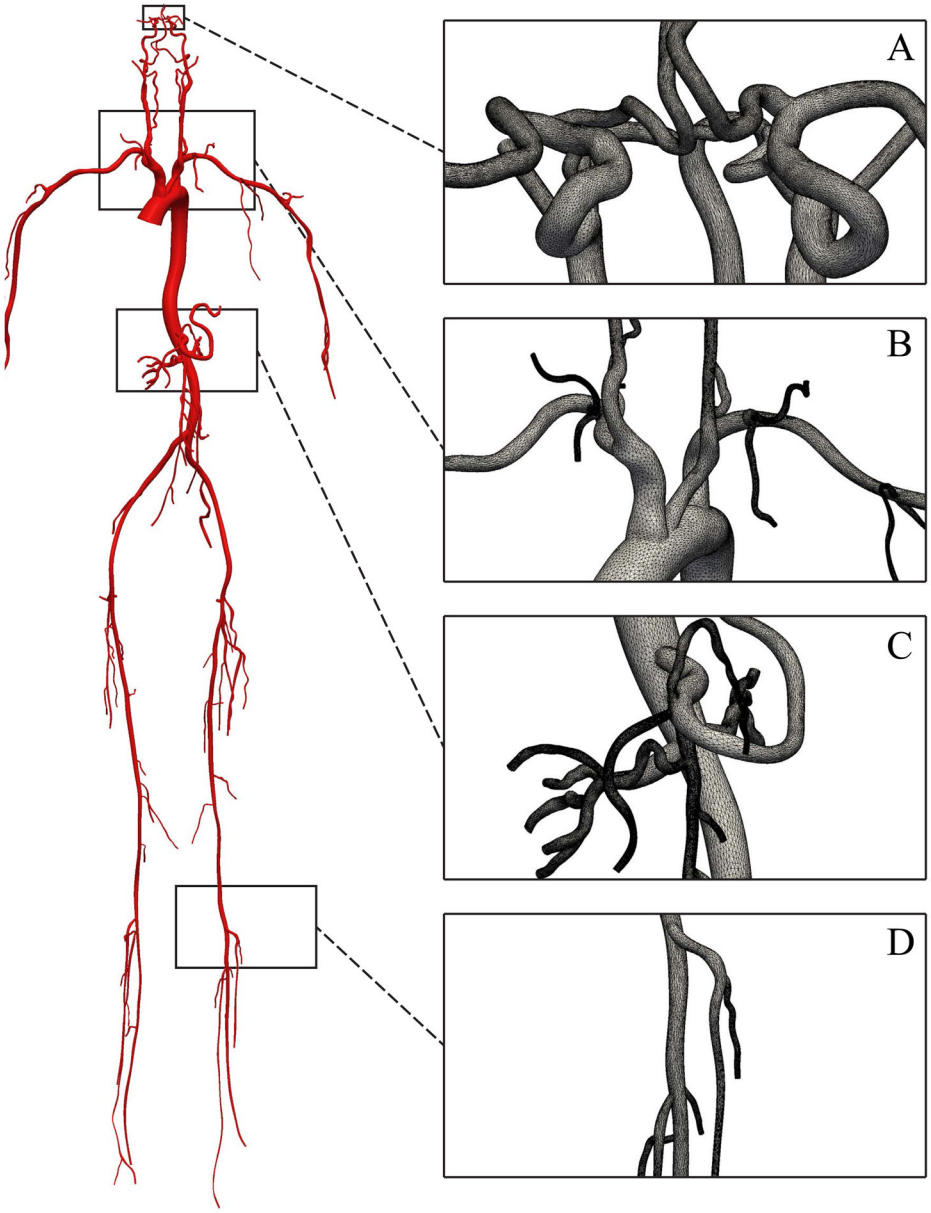

Figure 2.
The finite element mesh was generated by discretization of the 3-D solid model using curvature-based and field-based adaptive mesh refinement. Close-up views demonstrate greater element density in the smaller vessels.

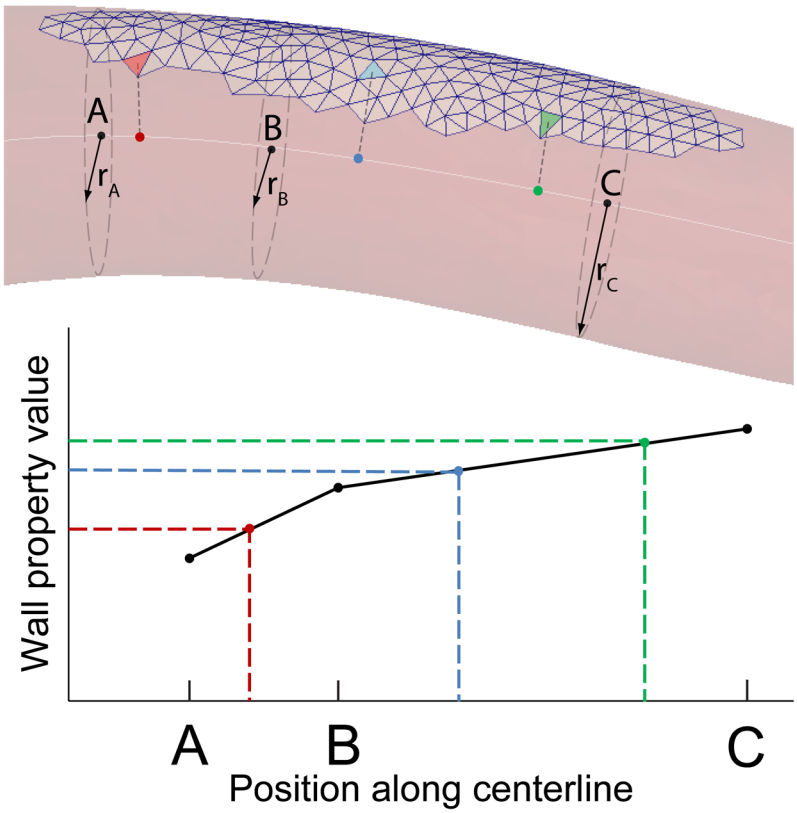

Figure 3.
Wall properties at discrete locations along the centerline were interpolated linearly and projected to the triangular elements of the vessel wall mesh.

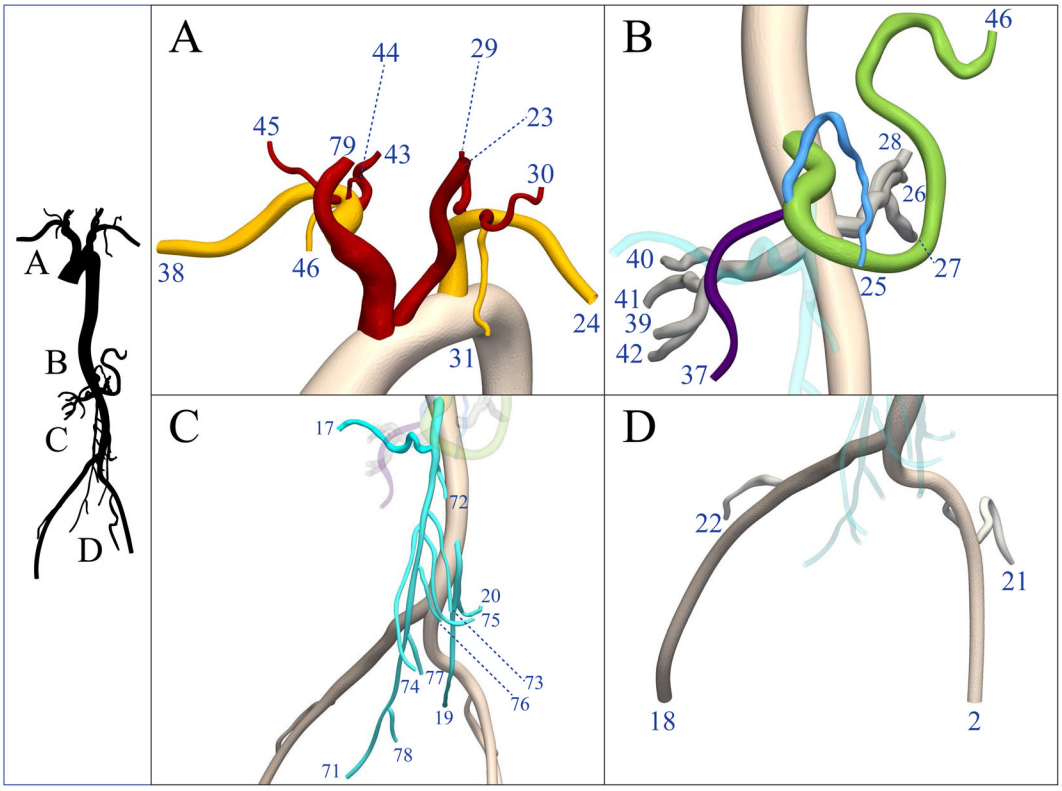

Figure 4.

Schematic of the outlet faces in the trunk model grouped by perfusion region. Close-up views depict the aortic arch vasculature (A), celiac trunk branches and renal arteries (B), mesenteric arteries (C), and iliac arteries (D). All outflow vessels are labeled with unique identifiers.

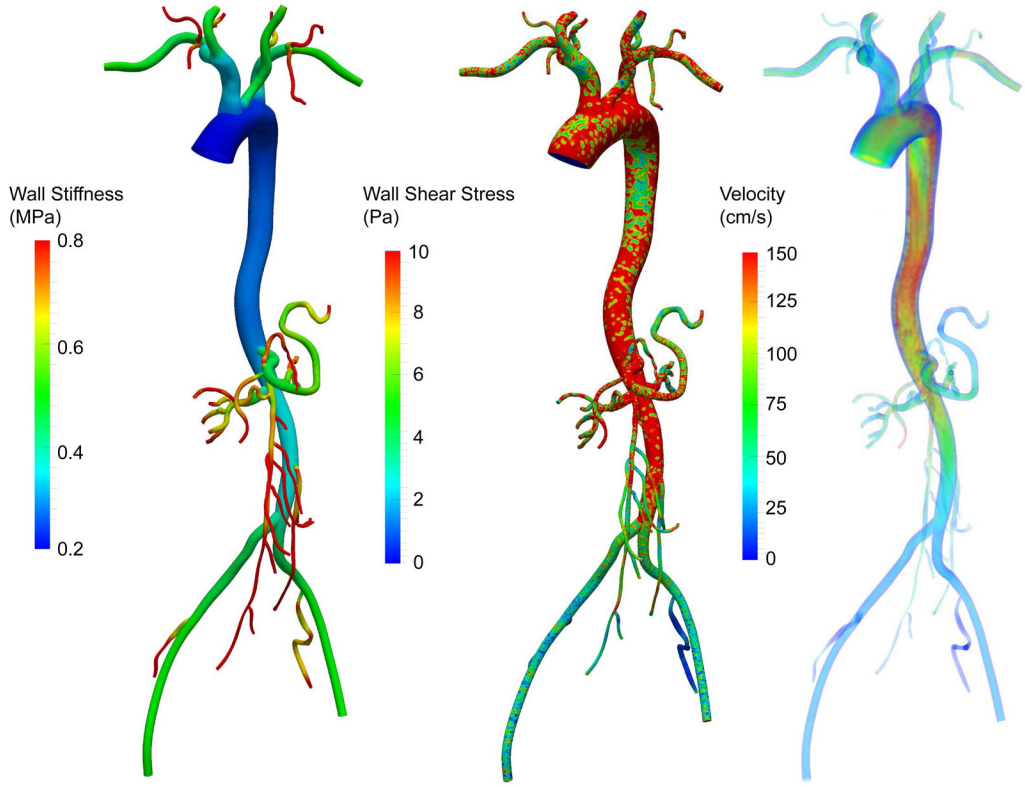

Figure 5.
From left to right: Wall stiffness, systolic wall shear stress and systolic velocity magnitude for the trunk model.

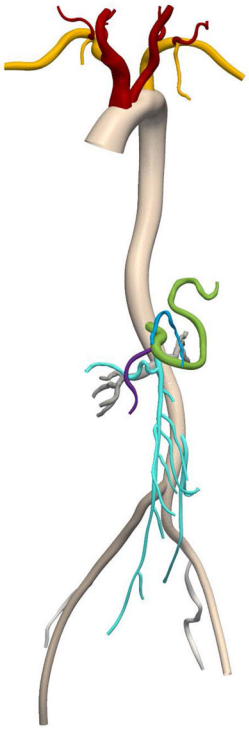

Location	% cardiac output (data)	% cardiac output (simulated)
Head	18.3	18.8
Arms	11.2	12.3
Spleen	3.2	3.2
Stomach	1.6	1.5
Mesenteric	17.3	16.1
Liver	7.6	5.8
Kidneys	18.4	18.8
Leg (Right)	11.2	11.7
Leg (Left)	11.2	11.9

Figure 6.
Comparison of regional flow distribution from literature data [46] with simulated regional flow distribution in the trunk model.

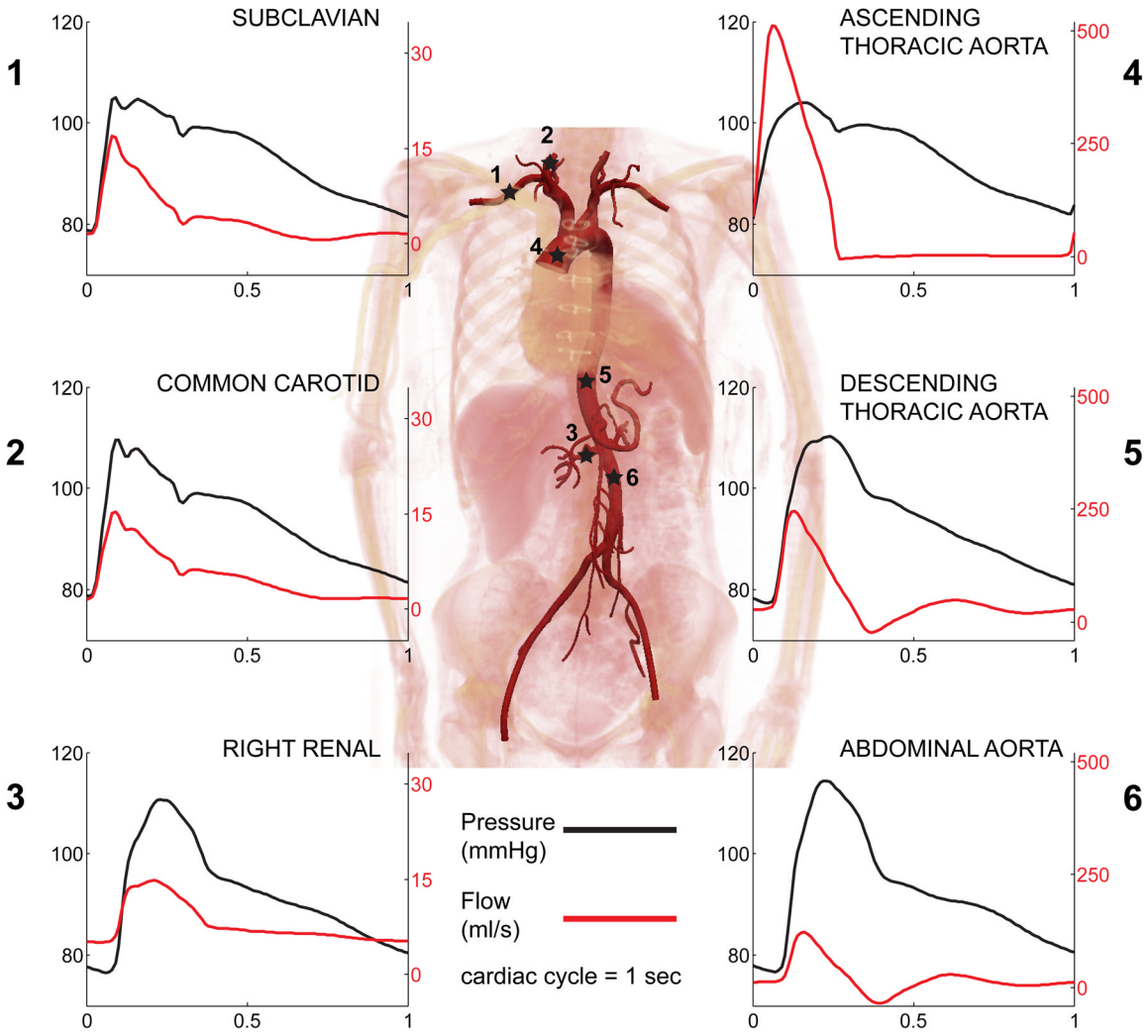

Figure 7.
Pressure and flow waveforms at multiple sites in the baseline “young” trunk model.

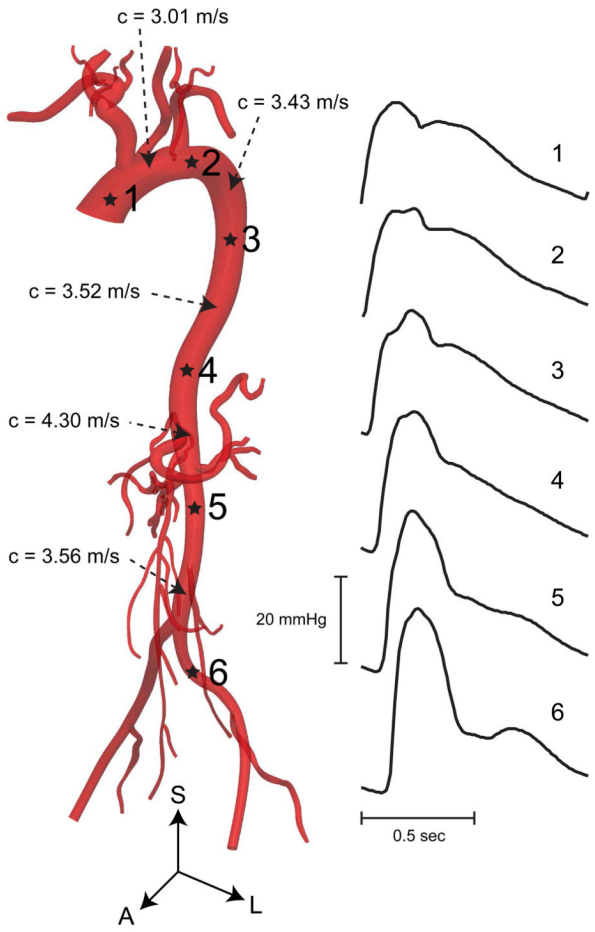

Figure 8.
Amplification of the pressure pulse and pressure wave velocity (PWV) down the aorta of the baseline "Young" trunk model.

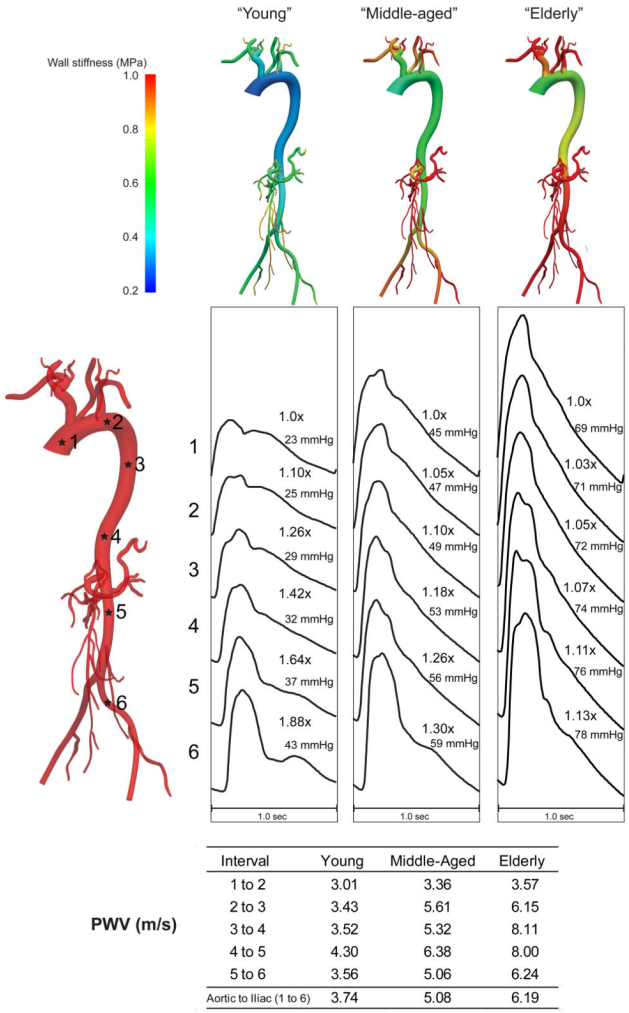

Interval	Young	Middle-Aged	Elderly
1 to 2	3.01	3.36	3.57
2 to 3	3.43	5.61	6.15
3 to 4	3.52	5.32	8.11
4 to 5	4.30	6.38	8.00
5 to 6	3.56	5.06	6.24
Aortic to Iliac (1 to 6)	3.74	5.08	6.19

Figure 9.

Top Panel: Distribution of arterial wall stiffness for three trunk cases. The "middle-aged" and "elderly" cases represent a 2x and 3x increase in arterial stiffness, respectively, over that of the "young" case. *Middle Panel*: Pressure waveforms at six sites in the aorta for all three cases. *Bottom Panel*: Comparison of pulse wave velocities between the three cases.

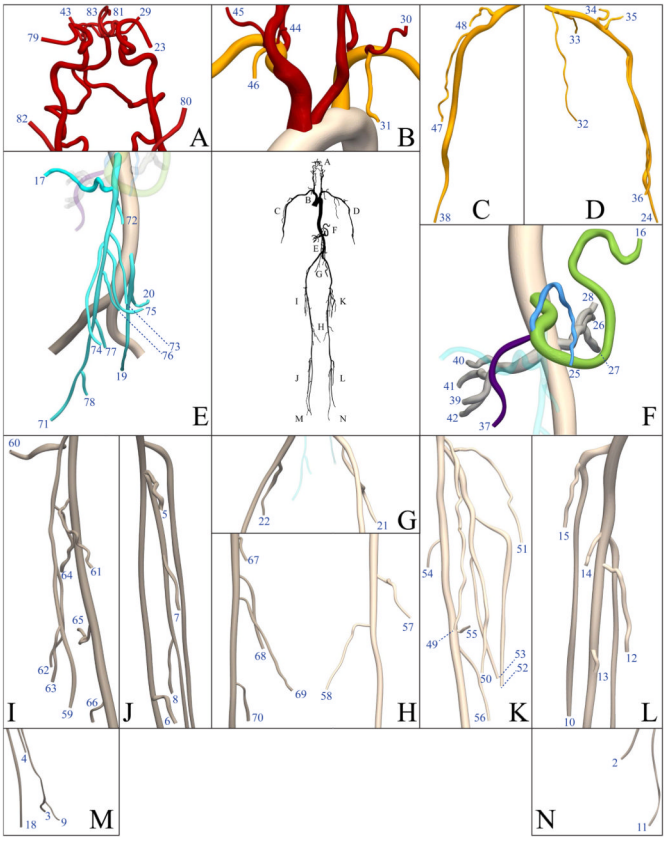

Figure 10.
Schematic of all arteries in the full-body model grouped by perfusion region. Close-up views depict the cerebral vasculature (A), subclavian branches (B), arm arteries (C,D), mesenteric branches (E), branches from the celiac trunk and the renal arteries (F), and the major leg arteries and their branches (I-N). All outflow vessels are labeled with unique identifiers.

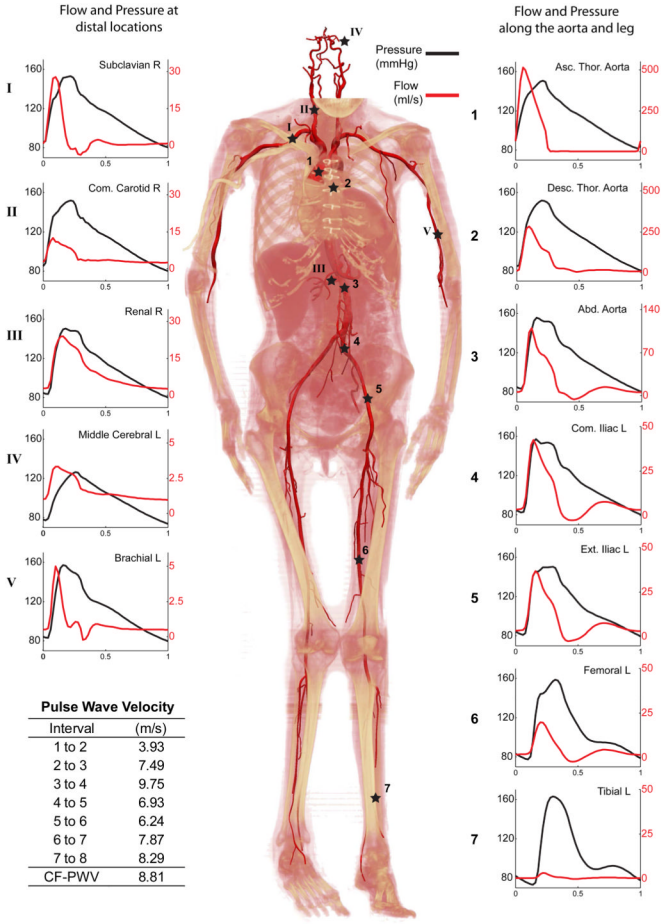

Pulse Wave Velocity

Interval	(m/s)
1 to 2	3.93
2 to 3	7.49
3 to 4	9.75
4 to 5	6.93
5 to 6	6.24
6 to 7	7.87
7 to 8	8.29
CF-PWV	8.81

Figure 11.

Pressure and flow waves at multiple sites in the full body model. Table shows PWV values obtained by measuring the time between the “foot” of the pressure waves at two sites. The calculated carotid-to-femoral pressure wave velocity (CF-PWV) is representative of typical values found in experimental measurements.

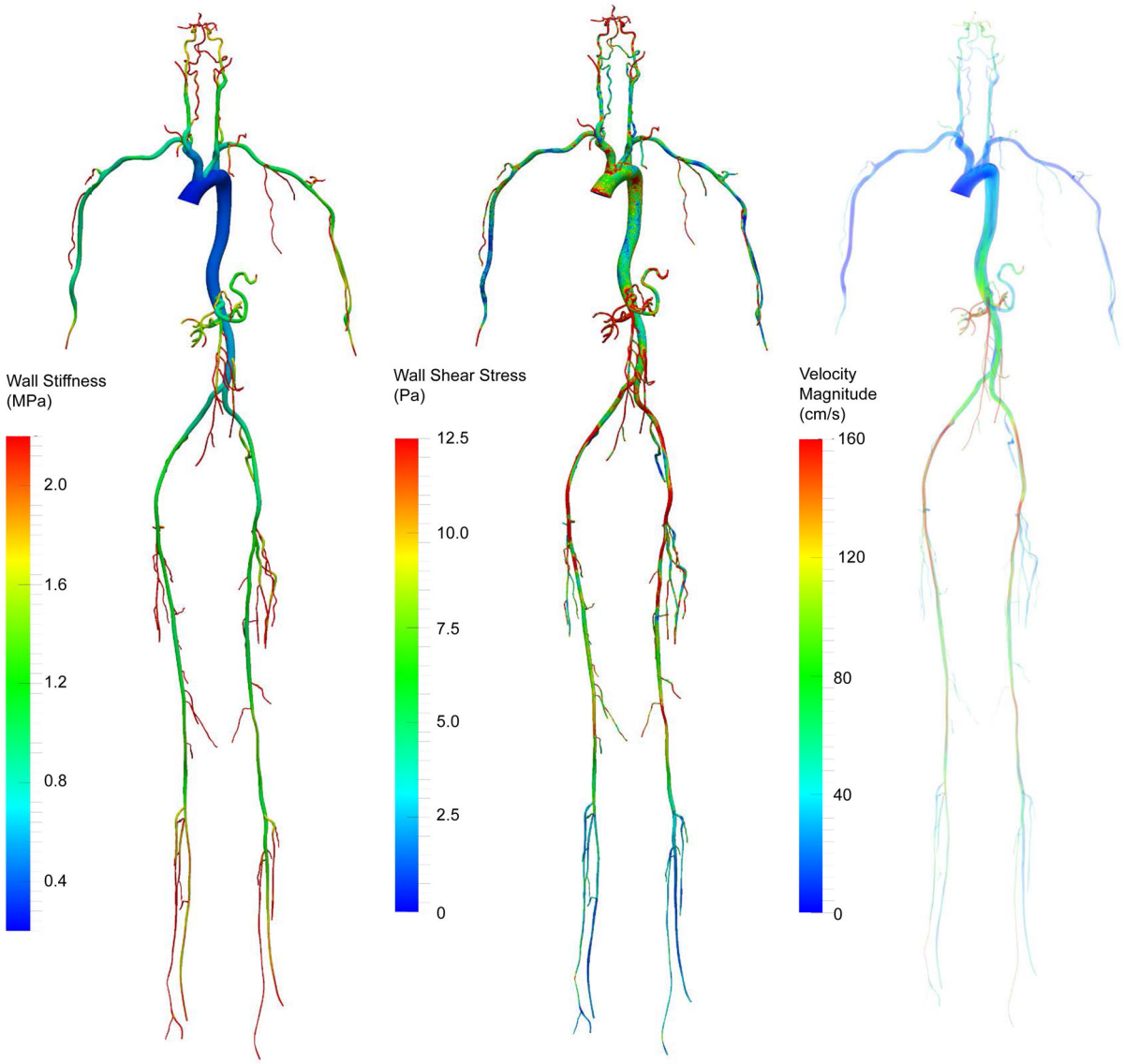

Figure 12.
From left to right: Regionally-varying wall stiffness, systolic wall shear stress and systolic velocity magnitude for the full-body-scale model.

Table 1

Windkessel parameters for the trunk model. R_p, C, R_d are the proximal resistance, compliance, and distal resistance respectively, and r is the equivalent radius, computed from the outlet cross-sectional area. The colors represent the different perfusion regions as depicted in Figure 4.

Face name	ID	R_p	C	R_d	r
Carotid L	23	2.60E+03	1.02E-04	2.34E+04	2.49
Carotid R	79	2.30E+03	1.15E-04	2.07E+04	2.65
Vertebral L	29	1.33E+04	9.95E-06	1.20E+05	1.10
Subclavian 1 L	30	1.33E+04	9.95E-06	1.20E+05	1.10
Vertebral R	43	9.56E+03	1.39E-05	8.60E+04	1.30
Subclavian 1 R	44	1.63E+04	8.11E-06	1.47E+05	1.00
Subclavian 2 R	45	1.63E+04	8.11E-06	1.47E+05	1.00
Subclavian L	24	1.75E+03	6.73E-05	2.94E+04	2.86
Subclavian 2 L	31	1.32E+04	8.90E-06	2.22E+05	1.04
Subclavian R	38	1.77E+03	6.62E-05	2.99E+04	2.83
Subclavian 3 R	46	1.09E+04	1.07E-05	1.84E+05	1.14
Splenic	16	2.65E+03	1.28E-05	4.46E+04	1.25
Left Gastric	25	5.29E+03	6.02E-06	8.92E+04	0.86
Hepatic	37	1.13E+03	9.95E-06	1.91E+04	1.10
Mid. Colic	17	2.73E+03	1.99E-05	4.61E+04	1.56
SMA 1	71	4.62E+03	1.18E-05	7.78E+04	1.20
SMA 2	72	6.70E+03	8.11E-06	1.13E+05	1.00
SMA 3	73	7.42E+03	7.33E-06	1.25E+05	0.94
SMA 4	74	6.70E+03	8.11E-06	1.13E+05	1.00
SMA 5	75	7.42E+03	7.33E-06	1.25E+05	0.94
SMA 6	76	9.04E+03	6.02E-06	1.52E+05	0.86
SMA 7	77	6.11E+03	8.90E-06	1.03E+05	1.04
SMA 8	78	6.70E+03	8.11E-06	1.13E+05	1.00
IMA 1	19	3.41E+03	1.60E-05	5.74E+04	1.39
IMA 2	20	6.70E+03	8.11E-06	1.13E+05	1.00
Renal 1 L	26	1.52E+04	1.44E-05	6.07E+04	1.32
Renal 2 L	27	9.60E+03	2.28E-05	3.84E+04	1.66
Renal 3 L	28	9.60E+03	2.28E-05	3.84E+04	1.66

Face name	ID	R_p	C	R_d	r
Renal 1 R	39	1.04E+04	2.09E-05	4.18E+04	1.60
Renal 2 R	40	1.55E+04	1.41E-05	6.19E+04	1.31
Renal 3 R	41	1.21E+04	1.81E-05	4.84E+04	1.48
Renal 4 R	42	1.21E+04	1.81E-05	4.84E+04	1.48
Ext. Iliac L	2	8.45E+02	2.87E-05	1.42E+04	3.74
Int. Iliac L	21	8.25E+03	2.94E-06	1.39E+05	1.20
Ext Iliac R	18	8.40E+02	2.81E-05	1.42E+04	3.70
Int Iliac R	22	8.79E+03	2.68E-06	1.48E+05	1.14

Table 2

Windkessel parameters for the full-body model. R_p, C, R_d are the proximal resistance, compliance, and distal resistance respectively, and r is the equivalent radius, computed from the outlet cross-sectional area. The colors represent the different perfusion regions as depicted in Figure 10.

Face name	ID	Rp	C	Rd	r
Ext. Carotid L	80	3.23E+03	6.84E-06	5.44E+04	1.22
Ext. Carotid R	82	3.53E+03	6.26E-06	5.95E+04	1.17
Subclavian 1 L	30	7.13E+03	5.53E-06	6.42E+04	1.10
Subclavian 1 R	44	8.74E+03	4.51E-06	7.86E+04	1.00
Subclavian 2 R	45	8.74E+03	4.51E-06	7.86E+04	1.00
Ant. Cerebral L	81	9.48E+03	2.33E-06	1.60E+05	0.71
Ant. Cerebral R	83	9.48E+03	2.33E-06	1.60E+05	0.71
Mid. Cerebral L	23	7.97E+03	4.95E-06	7.17E+04	1.04
Mid. Cerebral R	79	4.74E+03	4.66E-06	7.99E+04	1.01
Post. Cerebral L	29	1.59E+04	2.47E-06	1.43E+05	0.74
Post. Cerebral R	43	1.43E+04	2.77E-06	1.28E+05	0.78
Subclavian 2 L	31	8.64E+03	1.65E-06	1.46E+05	1.04
Axillary 1 L	32	1.05E+04	1.36E-06	1.77E+05	0.94
Axillary 2 L	33	8.64E+03	1.65E-06	1.46E+05	1.04
Axillary 3 L	34	1.28E+04	1.12E-06	2.15E+05	0.86
Axillary 4 L	35	1.63E+04	8.73E-07	2.75E+05	0.76
Brachial L	24	8.64E+03	1.65E-06	1.46E+05	1.04
Brachial 1 L	36	5.54E+03	2.57E-06	9.34E+04	1.30
Axillary 1 R	48	9.47E+03	1.50E-06	1.60E+05	1.00
Axillary 2 R	47	8.64E+03	1.65E-06	1.46E+05	1.04
Subclavian 3 R	46	7.16E+03	1.99E-06	1.21E+05	1.14
Brachial R	38	5.54E+03	2.57E-06	9.34E+04	1.30
Splenic	16	2.65E+03	1.43E-05	4.46E+04	1.25
Left Gastric	25	5.29E+03	6.70E-06	8.92E+04	0.86
Hepatic	37	1.13E+03	1.11E-05	1.91E+04	1.10
Mid. Colic	17	2.73E+03	2.21E-05	4.61E+04	1.56
SMA 1	71	4.62E+03	1.31E-05	7.78E+04	1.20
SMA 2	72	6.70E+03	9.02E-06	1.13E+05	1.00

Face name	ID	Rp	C	Rd	r
SMA 3	73	7.42E+03	8.15E-06	1.25E+05	0.94
SMA 4	74	6.70E+03	9.02E-06	1.13E+05	1.00
SMA 5	75	7.42E+03	8.15E-06	1.25E+05	0.94
SMA 6	76	9.04E+03	6.70E-06	1.52E+05	0.86
SMA 7	77	6.11E+03	9.90E-06	1.03E+05	1.04
SMA 8	78	6.70E+03	9.02E-06	1.13E+05	1.00
Renal 1 L	26	1.52E+04	1.60E-05	6.07E+04	1.32
Renal 2 L	27	9.60E+03	2.53E-05	3.84E+04	1.66
Renal 3 L	28	9.60E+03	2.53E-05	3.84E+04	1.66
Renal 1 R	39	1.04E+04	2.33E-05	4.18E+04	1.60
Renal 2 R	40	1.55E+04	1.57E-05	6.19E+04	1.31
Renal 3 R	41	1.21E+04	2.01E-05	4.84E+04	1.48
Renal 4 R	42	1.21E+04	2.01E-05	4.84E+04	1.48
IMA 1	19	3.41E+03	1.78E-05	5.74E+04	1.39
IMA 2	20	6.70E+03	9.02E-06	1.13E+05	1.00
Post. Tibial L	2	1.05E+04	1.24E-06	1.76E+05	1.04
Post. Tibial 1 L	12	1.55E+04	8.37E-07	2.61E+05	0.86
Post. Tibial 2 L	13	1.42E+04	9.10E-07	2.40E+05	0.89
Post. Tibial 3 L	14	1.98E+04	6.55E-07	3.33E+05	0.76
Int. Iliac L	21	7.91E+03	1.64E-06	1.33E+05	1.20
Ant. Tibial L	10	1.55E+04	8.37E-07	2.61E+05	0.86
Ant. Tibial 1 L	15	1.78E+04	7.28E-07	3.00E+05	0.80
Peroneal L	11	1.05E+04	1.24E-06	1.76E+05	1.04
SFA L	50	1.42E+04	9.10E-07	2.40E+05	0.89
SFA 1 L	49	1.27E+04	1.02E-06	2.14E+05	0.94
SFA 2 L	51	1.55E+04	8.37E-07	2.61E+05	0.86
SFA 3 L	52	1.05E+04	1.24E-06	1.76E+05	1.04
SFA 4 L	53	1.27E+04	1.02E-06	2.14E+05	0.94
SFA 5 L	54	1.78E+04	7.28E-07	3.00E+05	0.80
SFA 6 L	55	1.98E+04	6.55E-07	3.33E+05	0.76
SFA 7 L	56	1.55E+04	8.37E-07	2.61E+05	0.86

J Comput Phys. Author manuscript; available in PMC 2014 July 01.

Face name	ID	Rp	C	Rd	r
Popliteal 1 L	57	1.55E+04	8.37E-07	2.61E+05	0.86
Popliteal 2 L	58	1.78E+04	7.28E-07	3.00E+05	0.80
Post. Tibial R	18	8.80E+03	1.38E-06	1.48E+05	1.35
Int. Iliac R	22	1.22E+04	9.95E-07	2.06E+05	1.14
Ant. Tibial R	3	1.32E+04	9.22E-07	2.22E+05	1.10
Peroneal R	4	1.79E+04	6.79E-07	3.02E+05	0.94
Peroneal 1 R	5	1.62E+04	7.52E-07	2.73E+05	1.00
Post. Tibial 1 R	6	1.62E+04	7.52E-07	2.73E+05	1.00
Peroneal 2 R	7	2.18E+04	5.58E-07	3.68E+05	0.86
Peroneal 3 R	8	2.51E+04	4.85E-07	4.23E+05	0.80
Ant. Tibial 1 R	9	2.95E+04	4.12E-07	4.97E+05	0.74
SFA R	59	2.01E+04	6.06E-07	3.38E+05	0.89
SFA 1 R	60	1.32E+04	9.22E-07	2.22E+05	1.10
SFA 2 R	61	1.32E+04	9.22E-07	2.22E+05	1.10
SFA 3 R	62	2.79E+04	4.37E-07	4.70E+05	0.76
SFA 4 R	63	1.62E+04	7.52E-07	2.73E+05	1.00
SFA 5 R	64	1.62E+04	7.52E-07	2.73E+05	1.00
SFA 6 R	65	1.62E+04	7.52E-07	2.73E+05	1.00
SFA 7 R	66	1.62E+04	7.52E-07	2.73E+05	1.00
Popliteal 1 R	67	2.01E+04	6.06E-07	3.38E+05	0.89
Popliteal 2 R	68	1.62E+04	7.52E-07	2.73E+05	1.00
Popliteal 3 R	69	1.62E+04	7.52E-07	2.73E+05	1.00
Popliteal 4 R	70	1.32E+04	9.22E-07	2.22E+05	1.10